Supporting Information

Amino-functionalized Metal-Organic Framework for Efficient Separation of Xenon/Krypton

Bai-Xun He,[a†] Qian-Qian Xu,[a†] Xiyu Song,[a] Hao Zhuo,[a] Wen-Bin Li,[a] Rui-Biao Lin[a]* and Xiao-Ming Chen[a]

[a] MOE Key Laboratory of Bioinorganic and Synthetic Chemistry, School of Chemistry, Sun Yat-Sen University, Guangzhou 510275 (China)

† These authors contributed equally to this work.

* Corresponding author. Email: linruibiao@mail.sysu.edu.cn (Rui-Biao Lin)

1. Experimental procedures

1.1. Materials and characterization

All commercially available reagents and solvents were used without further purification. High-purity He (99.999%), Ar (99.999%) CO_2 (99.999%), N_2 (99.999%), Xe (99.99%) and/or Kr (99.99%) were used directly or after mixing for isotherm and column breakthrough experiment.

1.2. Synthesis of 1

Synthesis for microcrystals of **1**. 2.5 mmol 3-aminoisonicotinic acid was dissolved into a mixed solution of 40 mL DMA and 20 mL EtOH. An aqueous solution of 1 mmol $Cu(NO_3)_2$ in 5 mL water was added onto the mixed solution. The mixture was heated at 393 K for 36 h. The obtained green powder was filtered, washed with acetone, and was exchanged with methanol for 3 days.

Synthesis for single-crystals of **1**. 0.2 mmol 3-aminoisonicotinic acid was added into a glass tube, and a mixed solution of 3 mL EtOH and 6 mL DMA was added. Then an aqueous solution (0.5 mL) containing 0.1 mmol $Cu(NO_3)_2$ was added into the mixed solution. The mixture was heated at 373 K for 48 h. Green crystals were collected as products, some of them were suitable for single-crystal X-ray diffraction.

1.3. Single-Crystal X-Ray Diffraction Analyses

Single-Crystal X-Ray diffraction (SCXRD) data of **1** were collected at 100 K on the Rigaku XtaLab PRO MM007HF DW X diffractometer using monochromated Cu-Kα radiation. Data reduction and absorption correction were performed using CrysAlisPro software. The structure was solved with the direct method and refined with a full-matrix least-squares technique with the SHELXL software package. Anisotropic thermal parameters were used to refine all non-hydrogen atoms of the framework. Hydrogen atoms were generated geometrically and their positions were refined in the riding mode. In addition, the solvent mask routine was applied to remove the contributions to the scattering from the highly ordered solvent molecules. CCDC 2539386 contains the supplementary crystallographic data for this paper.

1.4. Powder X-ray Diffraction Analyses

Power X-Ray diffraction (PXRD) patterns were collected on the Rigaku Miniflex 600-C X diffractometer (Cu Kα) in the range of 2θ = 5-40°, which was used with scan speed of 10°/min and step size of 0.02° at 40 kV voltage and 15 mA current.

1.5. Thermogravimetry Analyses (TGA)

Thermogravimetry (TG) analyses were performed on the TG 209 F3 instrument from 25℃ to 700 ℃

with a ramp rate of 10°C min^{-1} under a nitrogen gas flow.

1.6. Gas Sorption Measurement

CO_2 sorption isotherms of **1** at 195 K were measured with an automatic volumetric adsorption apparatus ASAP 2020. Other sorption isotherms were measured on a BELSORP max II. Before the gas sorption experiment, the samples placed in the sample tube were activated under high vacuum at room temperature for 12 h. The test temperature was controlled by a liquid nitrogen bath (77 K), a dry ice-acetone bath (195 K), or a water bath (273-298 K).

1.7. Column Breakthrough Measurement

The column breakthrough tests were carried out using a self-built setup. Activated powder of **1** (0.76 g) was packed into a stainless-steel column with an internal diameter of 0.500 cm and a length of 15.0 cm. The column simulating the industrial fixed-bed was connected to the Gas Chromatography (Agilent Technologies 7890A) by stainless-steel pipes and placed in a temperature-controlled oven. Before introducing the indicated gas stream, the sample was further activated by purging the column with dry argon gas flow for 24 h at room temperature. The flow rates of gases were regulated by corrosion-resistant mass flow controllers. For the gas mixture for test, pure gases were mixed for at least 2 h with a total flow rate of 3 mL min^{-1} at 298 K. The gas stream at the outlet was collected by a six-way valve and analyzed online by an HP-AL/S (19095P–S25) chromatographic column and a thermal conductivity detector (TCD). The dead volume of the column packed with sample powder was calculated using the data from the thermal conductivity detector (TCD) by flushing the column with dry helium gas flow at the same flow rate with the gas mixture in one test. After the one breakthrough experiment, the sample was regenerated by flushing the column with dry argon gas flow at a flow rate of 1 mL min^{-1} until the intensities of the chromatographic peaks rapidly decreased to approximately equilibrium, after which the temperature of the oven was set to be 343 K at a default ramping rate (3–5°C min^{-1}).

To obtain net gas uptake of the material as accurately as possible, the gas retention in the pipeline should be calculated and deducted from the total gas retention calculated by integrating the breakthrough curve. The sampling setting of the six-way valve was used to measure the outlet flow rate instead of the concentration, thus the dead space of the breakthrough manifold could be determined as the equilibrium retention of the non-adsorbing He at the experimental conditions.

The specific injection amount (τ) in mmol g^{-1} as the abscissa was used for the breakthrough curve, which is derived from the following Eq. (1):

$$\tau = \frac{t}{V_{\mathrm{m}} \times m} \sum_{j=1}^{k} \upsilon_j \tag{1}$$

where t is the duration of the test (min); υ_j is the flow rate of gas j (mL min^{-1}) in the inlet gas mixture containing k kinds of gases; V_{m} is molar volume of gas at room temperature and 1 bar (24.5 L/mol), and m is mass of the activated sample (g).

The breakthrough curves for gas j are expressed by

$$f(j,\tau) = \frac{F_{\mathrm{o}}(j,\tau)}{F_{\mathrm{i}}(j)} \tag{2}$$

where $F_{\mathrm{o}}(j, \tau)$ is the TCD peak area of gas j at the outlet at τ and $F_{\mathrm{i}}(j)$ is the TCD peak area of gas j at the inlet which is equal to the equilibrium peak area (almost does not change with τ anymore).

The gas adsorption capacity or retention of gas j was calculated by Eq. (3) as follows:

$$r(j,\tau) = \frac{\upsilon_j}{\sum_{j=1}^{k} \upsilon_j} \int_0^{\tau} [1 - f(j,\tau)]\mathrm{d}\tau - \int_0^{\tau} [1 - f(l,\tau)]\mathrm{d}\tau \tag{3}$$

where $\int(0\rightarrow\tau)[1-f(l, \tau)]\mathrm{d}\tau$ means the gas retention in the pipeline in mmol g^{-1} which is approximate to the retention of the inert gas l tested before or after the gas j.

The instant purity u_{s} of gas j in the outlet gas mixture containing k kinds of gases can be expressed as

$$u_{\mathrm{s}} = \frac{f(j,\tau)}{\sum_{j=1}^{k} f(j,\tau)} \times 100\% \tag{4}$$

and the accumulated purity u_{a} of gas j should be determind by

$$u_{\mathrm{a}} = \frac{\int_{\tau_1}^{\tau_2} f(j,\tau)}{\sum_{j=1}^{k} \int_{\tau_1}^{\tau_2} f(j,\tau)} \times 100\% \tag{5}$$

The productivity y of gas j is defined as the effluent amount of gas j during a period from τ_1 to τ_2 where the accumulated purity u_{a} of gas j is higher than or equal to a required minimum value of 99.5%. That is

$$y = \int_{\tau_1}^{\tau_2} f(j,\tau)\,,\ u_a \geq 99.5\% \tag{6}$$

1.8. Analysis and Derivation of the Isosteric Heat of Adsorption

The isosteric heat of adsorption profiles of Xe and Kr were derived from adsorption isotherms measured at 273 K and 298 K by Virial fitting equation:

$$\ln p = \ln N + \frac{1}{T}\sum_{i=0}^{m} a_i N^i + \sum_{j=0}^{n} b_j N^j \tag{7}$$

$$Q_{st} = -R \times \sum_{i=0}^{m} a_i \times N^i \tag{8}$$

where p is the pressure (kPa); N is the amount adsorbed (mmol g^{-1}); a_i and b_j are Virial coefficients independent of temperature; T is the temperature (K); m and n are the the numbers of coefficients required to adequately describe the isotherms; R is the gas constant with a value of 8.314 J mol^{-1} K^{-1}.

1.9. Calculations of the ideal adsorption solution theory (IAST)

IAST was used to predict binary mixture adsorption from the experimental pure-gas isotherms. In order to perform the integrations required by IAST, the single-component isotherms were fitted by the dual-site Langmuir-Freundlich equation:

$$q = q_a \cdot \frac{b_a \cdot p^{v_a}}{1 + b_a \cdot p^{v_a}} + q_b \frac{b_b \cdot p^{v_b}}{1 + b_b \cdot p^{v_b}} \tag{9}$$

where p is the pressure of the bulk gas at equilibrium with the adsorbed phase (kPa), q is the adsorbed amount per mass of adsorbent (mmol g^{-1}), q_a, q_b is the saturation capacities of two sites (mmol g^{-1}), b_a, b_b is the affinity coefficients of two sites (kPa^{-1}), and v_a, v_b represents the deviations from ideal homogeneous surfaces.

Then the ideal adsorption selectivity is defined by:

$$S_{ads} = \frac{q_1/q_2}{p_1/p_2} \tag{10}$$

where q_1 and q_2 are the molar loadings in the adsorbed phase in equilibrium with the bulk gas phase with partial pressures p_1 and p_2.

1.10. Calculation of Henry's coefficient and selectivity

The calculation of Henry's constant can be derived from the virial equation expressed as follow:

$$ln(n/p) = A_0 + A_1 n + A_2 n^2 + \ldots \quad (11)$$

Where *P* is pressure, *n* is the amount adsorbed, and A_0, A_1, A_2... are virial coefficients. At low surface coverage, A_2 and A_3 can be neglected. The virial equation reduces to Henry's Law. However, the A_1 parameter for isotherms in the range 273-298 K was very small at low coverage and the isotherms were linear following Henry's Law:

$$n = K_H P \quad (12)$$

where *n* is the amount adsorbed in mmol/g, K_H is the Henry's constant and *P* is the pressure in bar.

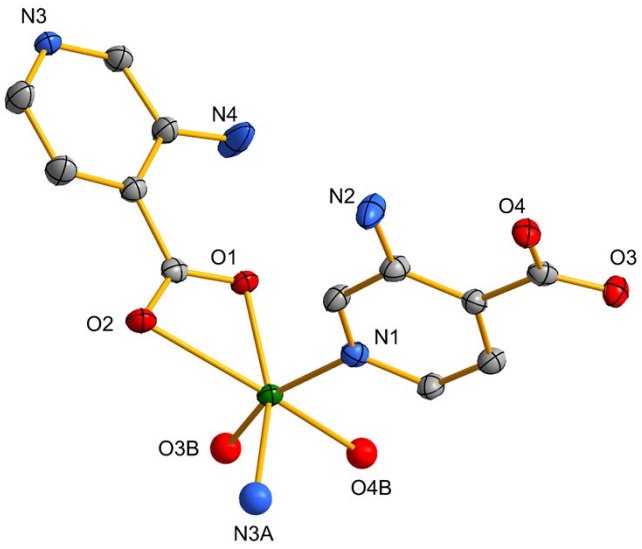

Fig. S1 Coordination environment of **1**. (symmetric codes: A = 1/2-*x*, 1-*y*, -1/2+*z*; B = 1-*x*, 1/2+*y*, 1/2-*z*). Hydrogen atoms are omitted for clarity.

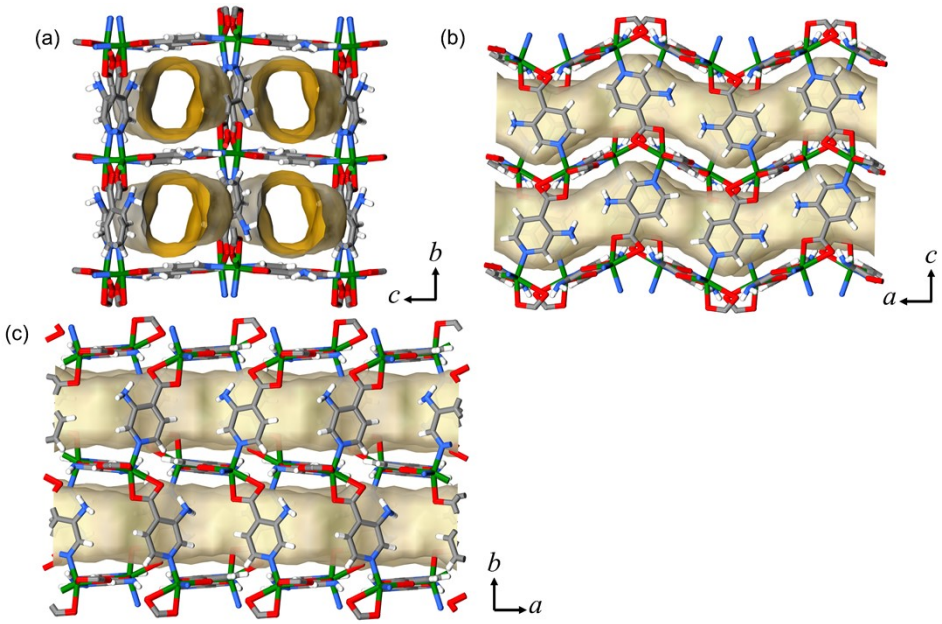

Fig. S2 The pore structure of **1** viewed along the *a*, *b* and *c* axis.

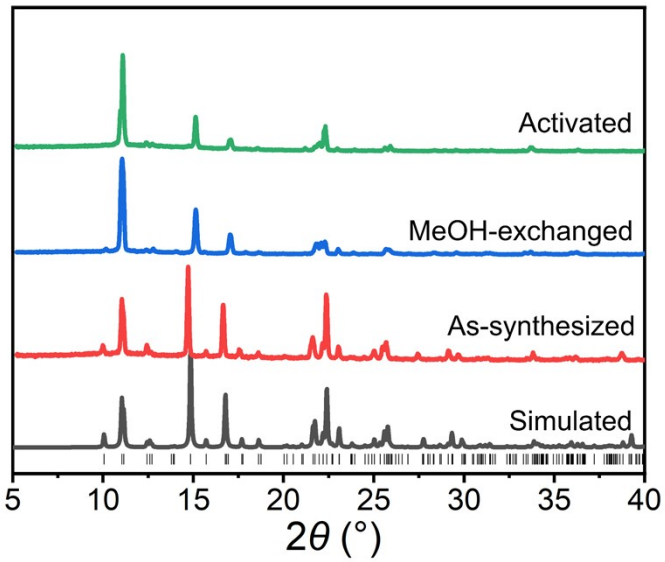

Fig. S3 PXRD patterns of as-synthesized (red), MeOH-exchanged (blue) and activated (green) samples of **1**.

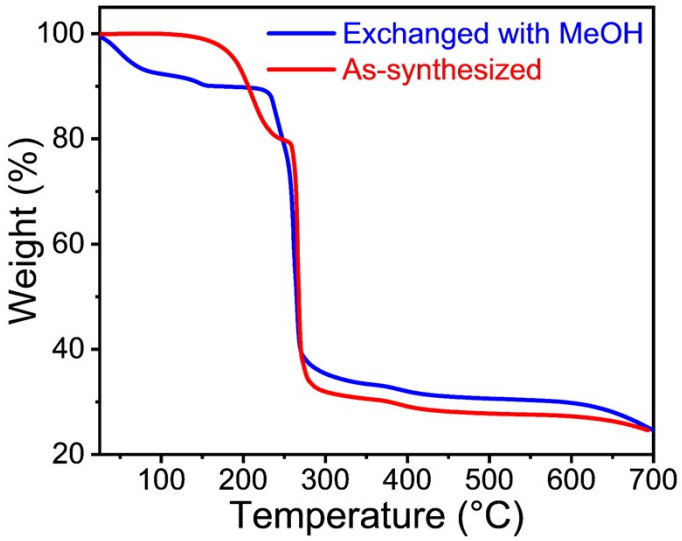

Fig. S4 TG curves of as-synthesized (red) and MeOH-exchanged (blue) samples of **1**.

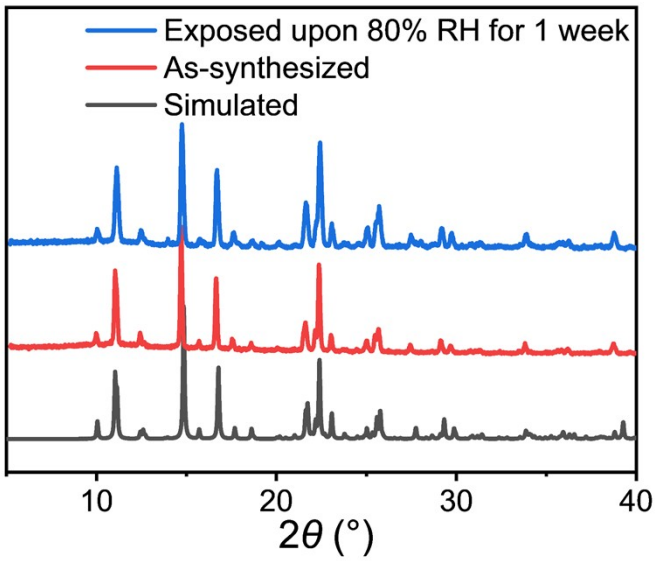

Fig. S5 PXRD patterns of **1** after exposure upon 80% RH for 1 week (blue).

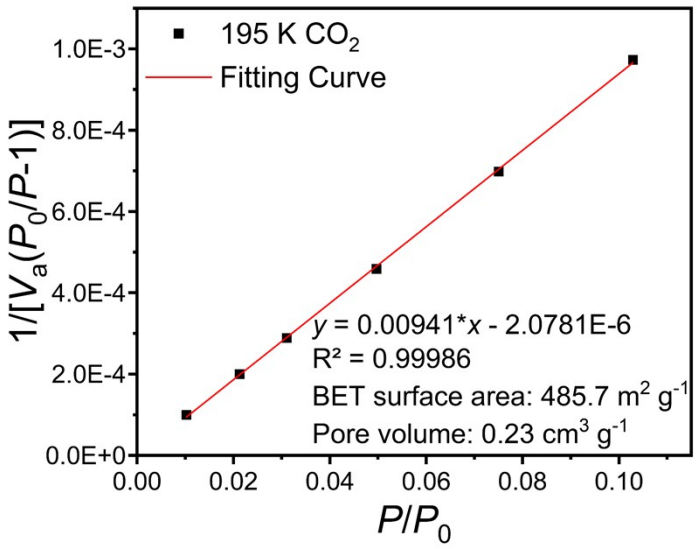

Fig. S6 BET calculation for **1**, based on CO_2 sorption isotherm at 195 K.

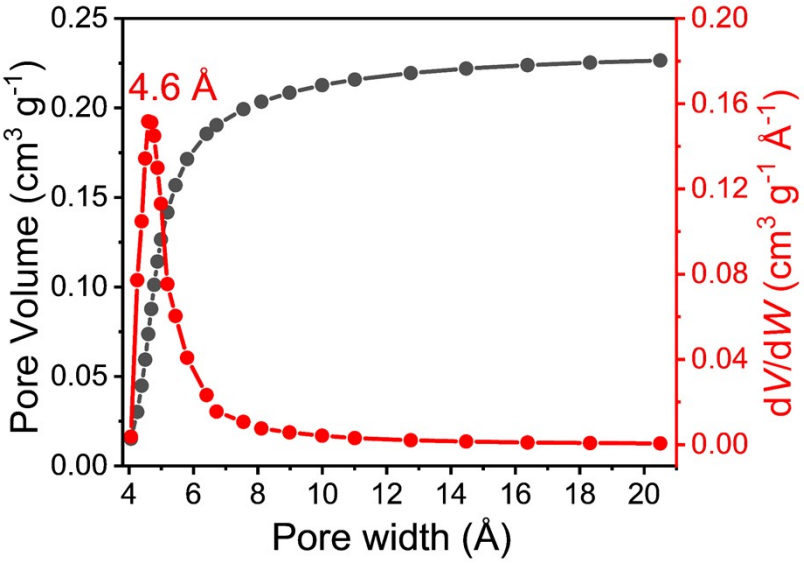

Fig. S7 Pore size distribution of **1**, calculated by Horvath-Kawazoe (H-K) method.

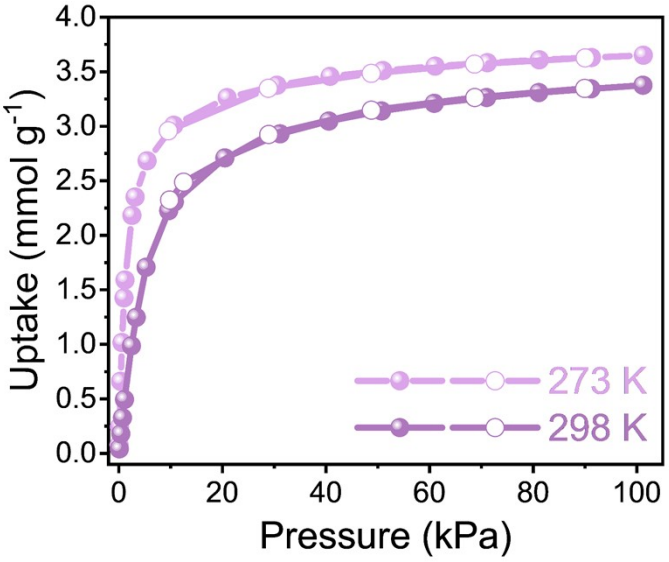

Fig. S8 Adsorption (solid) and desorption (open) isotherms of **1** for Xe at 273 and 298 K.

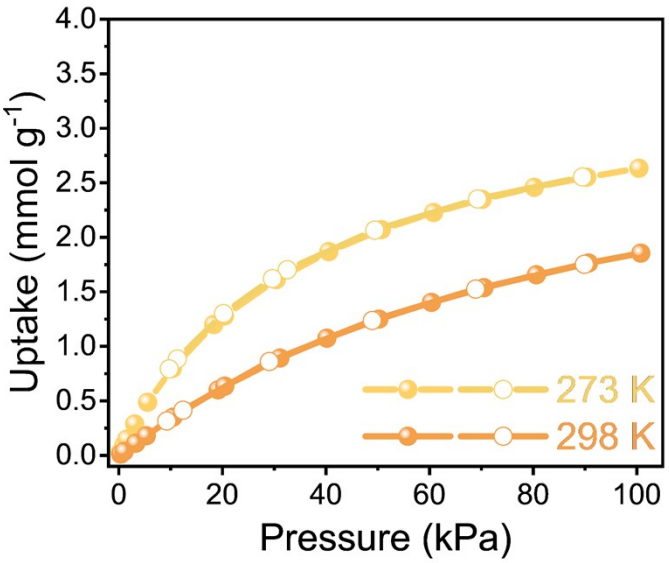

Fig. S9 Adsorption (solid) and desorption (open) isotherms of **1** for Kr at 273 and 298 K.

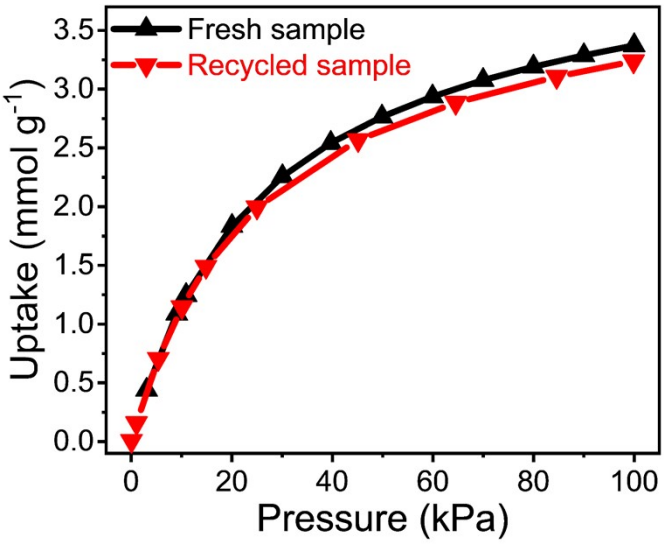

Fig. S10 Adsorption isotherms of fresh and recycled sample of **1** for CO_2 at 298 K.

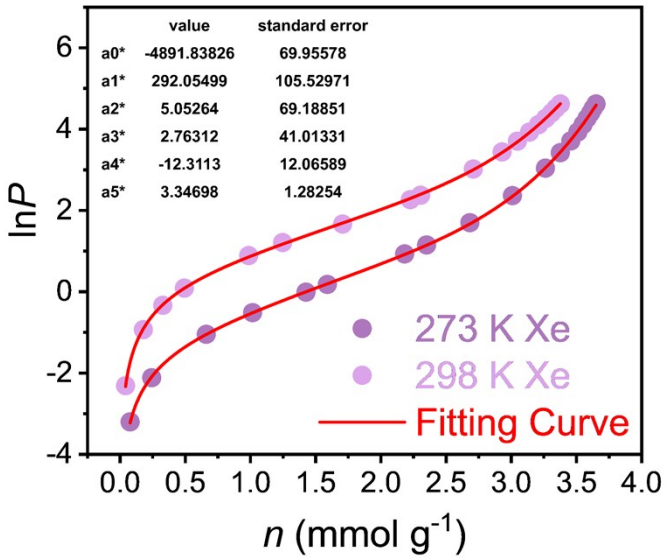

Fig. S11 Virial fitting curves of Xe.

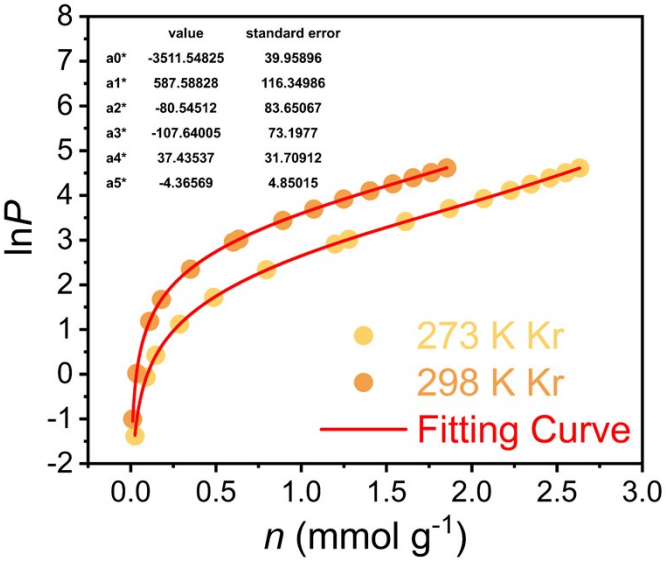

Fig. S12 Virial fitting curves of Kr.

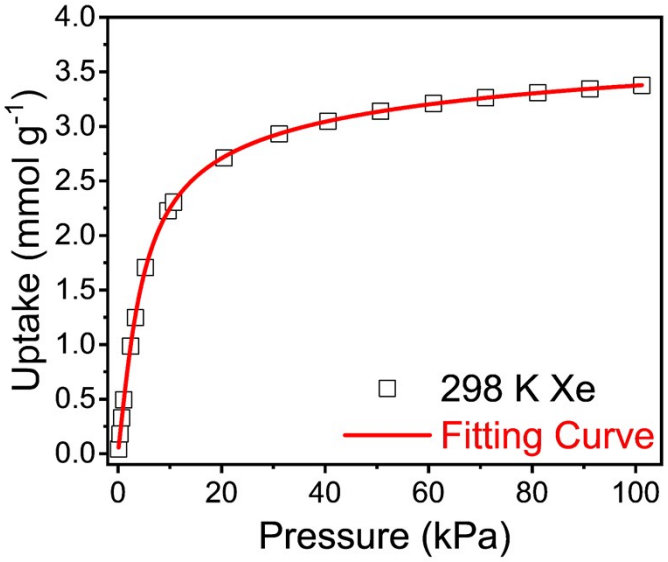

Fig. S13 Dual-site Langmuir Freundlich fitting of the Xe adsorption isotherm of **1** at 298 K.

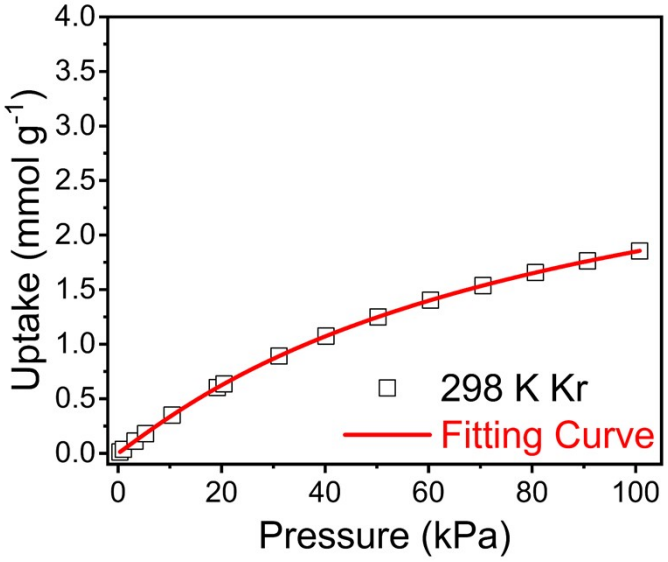

Fig. S14 Dual-site Langmuir Freundlich fitting of Kr adsorption isotherm of **1** at 298 K.

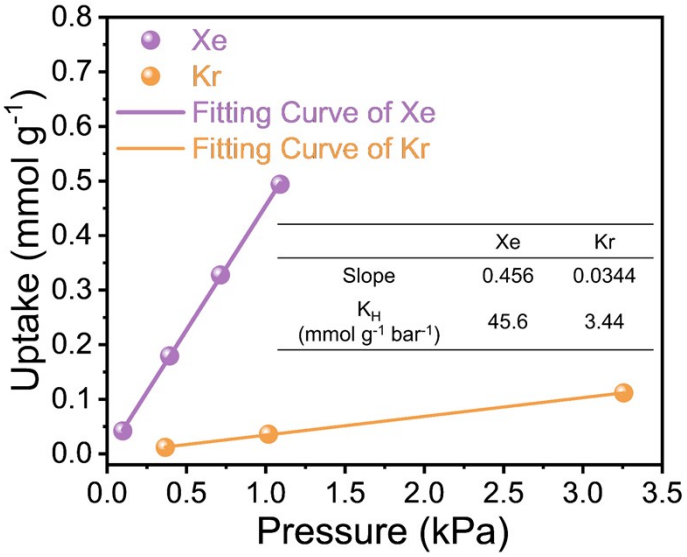

Fig. S15 Henry's coefficient of Xe and Kr in **1** at 298 K.

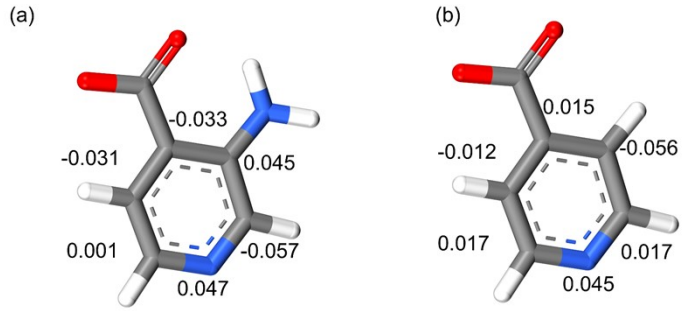

Fig. S16 Atomic charge distribution for fragment of (a) ain$^-$ ligand in **1** and (b) its non-substituted analogue.

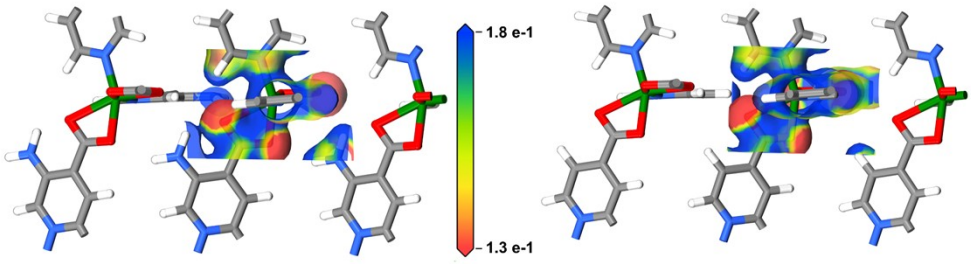

Fig. S17 Electrostatic potential surface of metal centers in **1** and its non-substituted analogue.

Table S1. Physical properties of Xe and Kr.

Adsorbate	Kinetic diameter (Å)	Boiling point (K)	Polarizability ($\times 10^{25}$ cm^3)
Xe	4.1	289.74	40.44
Kr	3.6	209.4	24.844

Table S2. Single-crystal diffraction data of **1·g**.

Compound	**1·g**
Formula	$C_{16}H_{19}CuN_5O_5$
Formula weight	424.90
Temperature (K)	100
Crystal system	orthorhombic
Space group	*Pbca*
a (Å)	14.0467(4)
b (Å)	15.8683(4)
c (Å)	16.0187(4)
V (Å^3)	3570.5(1)
Z	8
D_c (g cm^{-3})	1.581
μ (mm^{-1})	2.085
F(000)	1752
GooF	1.039
R_{int}	0.0308
R_1 [$I \geq 2\sigma(I)$]	0.0497
wR_2 [$I \geq 2\sigma(I)$]	0.1294
R_1 (all data)	0.0612
wR_2 (all data)	0.1374

[a] $R_1 = \Sigma||F_o| - |F_c||/\Sigma|F_o|$

[b] $wR_2 = [\Sigma w(F_o^2 - F_c^2)^2/\Sigma w(F_o^2)^2]^{1/2}$

Table S3. Fitting parameters for isotherms of Xe and Kr by dual-site Langmuir-Freundlich model (298 K and 100 kPa).

	q (mmol g^{-1})		b (kPa^{-1})		v		R^2
	q_a	q_b	b_a	b_b	v_a	v_b	
Xe	2.13227	1.94161	0.13986	0.10249	1.39619	0.63065	0.99992
Kr	0.07824	3.485	0.00513	0.00972	1.70826	1.01429	0.99999

Table S4. Comparison on sorption performance of **1** with relevant adsorbents for separation of Xe/Kr.

Adsorbents	Xe uptake (mmol g^{-1})		Q_{st} (Xe) (kJ mol^{-1})	IAST Selectivity (20/80, Xe/Kr)	K_H (Xe) (mmol g^{-1} bar^{-1})	T (K)	reference
	100 kPa	20 kPa					
1	**3.38**	**2.71**	**40.6**	**18.6**	**45.6**	**298**	**This Work**
$Ni(4\text{-dpds})_2CrO_4$	1.61	1.42	28.5	23.7	53.05	298	1
$Ni(4\text{-dpds})_2MoO_4$	1.07	0.94	32.8	20.3	39.21	298	1
$Ni(4\text{-dpds})_2WO_4$	1.11	0.99	34.5	30.2	22.78	298	1
NU-200	4.91	1.85	28	20.2	-	298	2
ZUL-C1	2.86	2.06	25	11.7	-	298	3
ZUL-C2	2.57	1.78	28	19.1	-	298	3
ZJU-74a-Ni	2.66	2.38	41.7	74.1	-	296	4
ZJU-74a-Pd	2.20	2.06	45.5	103.4	-	296	4
NU-1107-Ag(I)	2.77	1.37	34.6	13.4	10.39	298	5
SCU-11-A	3.17	0.98	-	5.7	4.81	298	6
Cu-MOF-303	3.19	1.42	24.4	8.2	-	298	7
Ag-MOF-303	3.27	1.79	28.2	10.4	-	298	7
MOF-Cu-H	3.19	2.64	33.41	16.7	39.75	298	8
Al-CDC	2.45	1.86	34.9	10.7	32.8	298	9
Cu-CDC	1.82	1.07	31.7	11.5	7.13	298	9
Ni-MOF	5.42	1.82	25	8.3	10	298	10
NKMOF-1-Ni	2.12	1.36	34.2	5.2	-	298	11
CopzNi	3.28	2.49	38.5	14.0	-	298	12
NipzNi	3.04	1.87	35.3	10.8	-	298	12
Cu-BTA	7.61	2.55	18.6	8.4	12.6	298	13
Zn-DMTDC-BPY	2.27	1.27	60	6.2	11.68	298	14
NKMOF-8-Br	3.79	3.39	36.6	16.7	53.8	298	15
NKMOF-8-Me	4.20	3.20	33.1	12.4	38.4	298	15
LIFM-DMOF-Cl_2	3.58	0.90	19.5	5.9	-	298	16
LIFM-DMOF-Br_2	3.12	0.99	20.77	7.5	-	298	16
MFM-520	1.73	0.95	29	35.0	-	298	17
LIFM-DMOF-Cl	3.00	0.59	18.28	4.9	-	298	18
LIFM-DMOF-Br	2.90	0.61	19.13	5.1	-	298	18
MOF-OH-DL	2.23	1.43	28.8	11.5	18.6	298	19
NNM-30	5.18	3.07	25.56	16.6	-	298	20
MIP-203-F-Br	1.30	0.95	30.6	10.8	27.2	298	21
MIP-203-F	2.14	1.44	36	9.4	23.3	298	22
MOF-801	1.72	0.78	25.3	7.6	7.8	298	23
Zr-fum-Me	1.90	1.05	30.9	11.8	17.4	298	23
FeMn-BTBP-F	3.30	1.02	22.3	6.6	13.1	298	24

NNM-21	2.46	1.54	27.5[a]	13.0	-	298	25
ZJU-Bao-302a	2.77	2.13	28.9	14.6	23.95	298	26
ZUL-530	3.13	2.55	30.5	20.5	32.4	298	27
Al-SDB	1.60	1.00	26	14.2	6.76	298	28
Ce-SINAP-1	2.02	0.80	24.2	14.9	10.0	293	29
$Co_3(HCOO)_6$	2.00	1.32	28	12.5	9.9	298	30
Co-squarate	1.35	1.18	43.6	69.7	192.1	298	31
CROFOUR-1-Ni	1.80	1.07	37.4	22.0	18.7	298	32
CROFOUR-2-Ni	1.60	0.84	30.5	15.5	15.95	298	32
Cu_{12}	1.21	0.62	30.5	10.4	-	296	33
ECUT-50	2.26	0.90	32	8.0	-	298	34
ECUT-51	2.70	1.28	32	5.6	8.22	298	35
ECUT-60	4.30	2.33	30	11.4	22	298	36
FJU-55	1.41	0.80	39.4	10.0	11.33	298	37
TIFSIX-Cu-TPA	2.88	0.86	22.3	5.4	-	298	38
HKUST-1	3.30	0.80	26.9	2.6	-	298	39
JXNU-11	3.26	0.85	19.5	5.6	4.09	298	40
JXNU-19	3.27	1.40	39.5	17.1	31.68	298	41
JXNU-20(Cl)	4.17	2.01	36.7	9.4	-	298	42
LPC-MOF	1.30	0.80	28	11.0	10	298	43
MIL-120	1.99	1.43	31.5	9.6	22.4	298	44
MIL-88B-tpt	6.06	1.70	27.1	7.8	-	298	45
Mn-dhbq	3.12	2.35	28.9	11.3	16.7	298	46
MOF-505	6.31	2.20	-	9.5	10.26	298	47
Ni_2(m-dobdc)	5.90	2.52	28.31	11.5	-	298	48
Ni-MOF-74	4.16	1.63	22	-	8.4	298	49
NU-1801	2.79	1.04	24.9	8.2	6.36	298	50
NU-403-PSDH	2.23	1.09	26	9.0	-	298	51
SBMOF-1	1.40	1.20	-	16.0	38.42	298	52
SBMOF-2	2.83	1.48	26.4	10.0	10.5	298	53
SIFSIX-3-Cu	2.11	0.98	45.93[b]	4.8	-	298	54
SIFSIX-3-Fe	2.45	1.34	27.4	-	-	298	55
SIFSIX-3-Ni	2.51	0.54	21	-	-	298	55
Uio-66(Zr)	1.58	0.53	25	6.7	3.56	303	56
UTSA-49	3.00	0.30	23.53	9.2	-	298	57
UTSA-74	2.71	0.91	24.4	10.4	-	298	58
$Zn(ox)_{0.5}$(trz)	2.72	1.89	29	10.2	15.8	298	59
ZU-62	3.76	0.20	35.2[b]	-	-	298	60
$Ni(AIN)_2$	2.97	2.56	30.95	20.3	107.6	298	61
ATC-Cu	5.00	3.97	39.38 (Xe1)[c] 41.56 (Xe2)[c]	13.9	-	298	62
JXNU-13-F	3.72	0.92	31.5	6.8	4.61	273	63
BUT-422	3.19	2.91	33.2	22.5	-	298	64
$Mn(ina)_2$	1.65	0.03	26.5	114[d]	-	298	65

"-" means this data is not available in the references.

[a] calculated at 7 $cm^3 g^{-1}$.

[b] determined by DFT calculations.

[c] determined by DFT-D calculations

[d] under Xe/Kr (50/50, *v*/*v*) mixtures

References

[1] F. Zheng, L. Guo, R. Chen, L. Chen, Z. Zhang, Q. Yang, Y. Yang, B. Su, Q. Ren and Z. Bao, Shell-like Xenon Nano-Traps within Angular Anion-Pillared Layered Porous Materials for Boosting Xe/Kr Separation, *Angew. Chem. Int. Ed.*, 2022, **61**, e202116686.

[2] W. Gong, Y. Xie, T. D. Pham, S. Shetty, F. A. Son, K. B. Idrees, Z. Chen, H. Xie, Y. Liu, R. Q. Snurr, B. Chen, B. Alameddine, Y. Cui and O. K. Farha, Creating Optimal Pockets in a Clathrochelate-Based Metal–Organic Framework for Gas Adsorption and Separation: Experimental and Computational Studies, *J. Am. Chem. Soc.*, 2022, **144**, 3737-3745.

[3] J. Zhou, T. Ke, F. Steinke, N. Stock, Z. Zhang, Z. Bao, X. He, Q. Ren and Q. Yang, Tunable Confined Aliphatic Pore Environment in Robust Metal–Organic Frameworks for Efficient Separation of Gases with a Similar Structure, *J. Am. Chem. Soc.*, 2022, **144**, 14322-14329.

[4] J. Pei, X.-W. Gu, C.-C. Liang, B. Chen, B. Li and G. Qian, Robust and Radiation-Resistant Hofmann-Type Metal–Organic Frameworks for Record Xenon/Krypton Separation, *J. Am. Chem. Soc.*, 2022, **144**, 3200-3209.

[5] W. Gong, Y. Xie, X. Wang, K. O. Kirlikovali, K. B. Idrees, F. Sha, H. Xie, Y. Liu, B. Chen, Y. Cui and O. K. Farha, Programmed Polarizability Engineering in a Cyclen-Based Cubic Zr(IV) Metal–Organic Framework to Boost Xe/Kr Separation, *J. Am. Chem. Soc.*, 2023, **145**, 2679-2689.

[6] Y. Wang, W. Liu, Z. Bai, T. Zheng, M. A. Silver, Y. Li, Y. Wang, X. Wang, J. Diwu, Z. Chai and S. Wang, Employing an Unsaturated Th^{4+} Site in a Porous Thorium–Organic Framework for Kr/Xe Uptake and Separation, *Angew. Chem. Int. Ed.*, 2018, **57**, 5783-5787.

[7] H. Wang, Z. Shi, J. Yang, T. Sun, B. Rungtaweevoranit, H. Lyu, Y.-B. Zhang and O. M. Yaghi, Docking of CuI and AgI in Metal–Organic Frameworks for Adsorption and Separation of Xenon, *Angew. Chem. Int. Ed.*, 2021, **60**, 3417-3421.

[8] S. Xiong, Y. Gong, S. Hu, X. Wu, W. Li, Y. He, B. Chen and X. Wang, A microporous metal–organic framework with commensurate adsorption and highly selective separation of xenon, *J. Mater. Chem. A*, 2018, **6**, 4752-4758.

[9] Z. Zhu, B. Li, X. Liu, P. Zhang, S. Chen, Q. Deng, Z. Zeng, J. Wang and S. Deng, Efficient Xe/Kr separation on two Metal-Organic frameworks with distinct pore shapes, *Sep. Purif. Technol.*, 2021, **274**, 119132.

[10] G. Li, G. Ji, X. Wang, W. Liu, D. Zhang, L. Chen, L. He, S. Liang, X. Li, F. Ma and S. Wang, Efficient and selective capture of xenon over krypton by a window-cage metal–organic framework with parallel aromatic rings, *Sep. Purif. Technol.*, 2022, **295**, 121281.

[11] T. Wang, Y.-L. Peng, E. Lin, Z. Niu, P. Li, S. Ma, P. Zhao, Y. Chen, P. Cheng and Z. Zhang, Robust Bimetallic Ultramicroporous Metal–Organic Framework for Separation and Purification of Noble Gases, *Inorg. Chem.*, 2020, **59**, 4868-4873.

[12] L. Guo, F. Zheng, Q. Xu, R. Chen, H. Sun, L. Chen, Z. Zhang, Q. Yang, Y. Yang, Q. Ren and Z. Bao, Double-Accessible Open Metal Sites in Metal–Organic Frameworks with Suitable Pore Size for Efficient Xe/Kr Separation, *Ind. Eng. Chem. Res.*, 2022, **61**, 7361-7369.

[13] X. Cui, J. Yue, H. Li, Y. Zhang, H. Huang, H. Yang and L. Gan, Boosting Record Xe Uptake for Efficient Xe/Kr Separation under High Humidity in a Cage-Based MOF with Open Metal Sites,

Inorg. Chem., 2026, **65**, 873-880.

[14] Z. Lu, Y. Gu, Y. Ding and F. Li, Synergistic confinement and polar recognition in a methyl-engineered ultramicroporous MOF for boosted Xe/Kr separation, *Chem. Eng. J.*, 2025, **525**, 170325.

[15] Y. Liu, Z. Zhou, W. Xia, F. Zheng, Z. Zhang, Q. Yang, Q. Ren and Z. Bao, Biomimetic Hydrophobic-Polar Metal-Organic Frameworks for Record-Breaking Separation and Capture of Xenon and Krypton, *Angew. Chem. Int. Ed.*, 2025, **64**, e20094.

[16] D. Yue, R.-M. Li, L. Yan, X.-Y. Zhu, M. Barboiu, H.-P. Wang, Z.-W. Wei, C.-Y. Su and J.-J. Jiang, Polarization-enhanced molecular traps: Halogen-functionalized MOFs achieve Xe/Kr separation via synergistic pore confinement and surface polarization, *Sep. Purif. Technol.*, 2026, **381**, 135591.

[17] T. D. Duong, J. Li, R. Li, X. Lian, Y. Chen, J. Fan, J. Hurd, L. Guo, D. Lee, M. Warren and S. Yang, Efficient Capture and Separation of Xenon/Krypton from Off-Gas by a Radiation-Resistant Metal–Organic Framework, *Small*, 2025, **21**, e08918.

[18] D. Yue, R.-M. Li, H.-T. Zheng, L. Yan, L. Song, R. Langer, M. Barboiu, Z.-W. Wei, J.-J. Jiang and C.-Y. Su, Optimizing Pore Size and Polarity in Halogen-Functionalized Metal–Organic Frameworks for Efficient Xenon/Krypton Separation: A Synergistic Strategy, *ACS Appl. Mater. Interfaces*, 2025, **17**, 36252-36259.

[19] B. Liu, S. Dong, K. Lv, Z. Liu, S. Qi, S. Xiong and S. Hu, Geometrical pore engineering via ligand racemization in metal–organic frameworks for enhanced Xe capture and separation, *J. Mater. Chem. A*, 2025, **13**, 12195-12202.

[20] Y. Qi, C. Xue, Y. Zhang, Y. Huang, H. Huang, L. Gan and H. Yang, Nonpolar Pore Confinement within Metal–Organic Frameworks for Xe/Kr Separation, *ACS Materials Lett.*, 2025, **7**, 1488-1495.

[21] S. Dong, B. Liu, K. Lv, S. Hu, Z. Liu, Z. Mao and S. Xiong, Bromine functionalized zirconium–fumarate frameworks for enhanced xenon capture and separation, *Sep. Purif. Technol.*, 2025, **363**, 132282.

[22] R. Chen, B. Sheng, F. Zheng, J. Li, H. Sun, F. Zhou, L. Chen, Z. Zhang, Q. Yang, Q. Ren and Z. Bao, Topology and porosity control on zirconium–fumarate frameworks boosting xenon/krypton separation, *AICHE J.*, 2023, **69**, e18169.

[23] Z. Yan, Y. Gong, B. Chen, X. Wu, Q. liu, L. Cui, S. Xiong and S. Peng, Methyl functionalized Zr-Fum MOF with enhanced Xenon adsorption and separation, *Sep. Purif. Technol.*, 2020, **239**, 116514.

[24] X. Fu, Q. Chen, J. Zhu, W. Su and X. Yang, Fluoro-functionalized metal organic frameworks with two-fold interpenetration for boosting xenon/krypton separation, *Chem. Eng. J.*, 2024, **502**, 158141.

[25] C. Xue, Y. Zhang, K. Qu, S. Gong and H. Yang, Stable Microporous Metal–Organic Framework Based on Tritopic Pyrazolate Ligand for Xe/Kr Separation, *Inorg. Chem.*, 2024, **63**, 23459-23466.

[26] Z. Zhou, W. Xia, Y. Liu, W. Shi, Y. Gao, Z. Zhang, Q. Yang, Q. Ren and Z. Bao, Ultramicroporous Metal–Organic Framework Featuring Multiple Polar Sites for Efficient Xenon Capture and Xe/Kr Separation, *ACS Appl. Mater. Interfaces*, 2024, **16**, 66358-66366.

[27] X. Zhu, T. Ke, P. Han, Z. Zhang, Z. Bao, Y. Yang, Q. Ren and Q. Yang, Pore Chemistry and Architecture Control in Anionic Functional Ultramicroporous Materials for Record Dense

Packing of Xenon, *J. Am. Chem. Soc.*, 2024, **146**, 24956-24965.

[28] M.-B. Kim, A. J. Robinson, M. L. Sushko and P. K. Thallapally, Aluminum-based microporous metal–organic framework for noble gas separation, *J. Ind. Eng. Chem.*, 2023, **118**, 181-186.

[29] X. Wu, Z.-J. Li, H. Zhou, L. Li, Z. Qian, N. Qian, X. Chu and W. Liu, A microporous Ce-based MOF with the octahedron cage for highly selective adsorption towards xenon over krypton, *RSC Adv.*, 2021, **11**, 30918-30924.

[30] H. Wang, K. Yao, Z. Zhang, J. Jagiello, Q. Gong, Y. Han and J. Li, The first example of commensurate adsorption of atomic gas in a MOF and effective separation of xenon from other noble gases, *Chem. Sci.*, 2014, **5**, 620-624.

[31] L. Li, L. Guo, Z. Zhang, Q. Yang, Y. Yang, Z. Bao, Q. Ren and J. Li, A Robust Squarate-Based Metal–Organic Framework Demonstrates Record-High Affinity and Selectivity for Xenon over Krypton, *J. Am. Chem. Soc.*, 2019, **141**, 9358-9364.

[32] M. H. Mohamed, S. K. Elsaidi, T. Pham, K. A. Forrest, H. T. Schaef, A. Hogan, L. Wojtas, W. Xu, B. Space, M. J. Zaworotko and P. K. Thallapally, Hybrid ultra-microporous materials for selective xenon adsorption and separation, *Angew. Chem. Int. Ed.*, 2016, **55**, 8285-8289.

[33] X. Fan, K. Zuo, F. Yuan, Y. Li, L. Li, S. Lin, J. Huang, S. Xiang, J.-Q. Wang and Z. Zhang, High-Nuclear Alkynyl Cu(I) Cluster-Based Framework for Efficient Xe/Kr Separation, *ACS Materials Lett.*, 2024, **6**, 1007-1011.

[34] L. Wang, W. Liu, J. Ding, H. Zhang, Y. Zhu and F. Luo, A Robust Calcium–Organic Framework for Effective Separation of Xenon and Krypton, *Cryst. Growth Des.*, 2021, **21**, 954-959.

[35] L. Wang, J. Ding, Y. Zhu, Z. Xu, Y. Fan, R. Krishna and F. Luo, A robust metal-organic framework showing two distinct pores for effective separation of xenon and krypton, *Micropor. Mesopor. Mat.*, 2021, **326**, 111350.

[36] H. Zhang, Y. Fan, R. Krishna, X. Feng, L. Wang and F. Luo, Robust metal–organic framework with multiple traps for trace Xe/Kr separation, *Sci. Bull.*, 2021, **66**, 1073-1079.

[37] L. Gong, Y. Liu, J. Ren, A. M. Al-Enizi, A. Nafady, Y. Ye, Z. Bao and S. Ma, Utilization of cationic microporous metal-organic framework for efficient Xe/Kr separation, *Nano Res.*, 2022, **15**, 7559-7564.

[38] J. Li, L. Wang, Y. Chen, Z. Gu, T. Jiang, B. Luan, R. Krishna and Y. Zhang, Efficient Xe/Kr separation in fluorinated pillar-caged metal-organic frameworks, *Micropor. Mesopor. Mat.*, 2023, **357**, 112631.

[39] A. Soleimani Dorcheh, D. Denysenko, D. Volkmer, W. Donner and M. Hirscher, Noble gases and microporous frameworks; from interaction to application, *Micropor. Mesopor. Mat.*, 2012, **162**, 64-68.

[40] X.-P. Fu, Z.-R. Li, Q.-Y. Liu, H. Guan and Y.-L. Wang, Microporous Metal–Organic Framework with Cage-within-Cage Structures for Xenon/Krypton Separation, *Int. Eng. Chem. Res.*, 2022, **61**, 7397-7402.

[41] D.-M. Zeng, L. Huang, X.-P. Fu, Y.-L. Wang, J. Chen and Q.-Y. Liu, Metal–Organic Frameworks Possessing Suitable Pores for Xe/Kr Separation, *Inorg. Chem.*, 2024, **63**, 5151-5157.

[42] K.-A. Zhou, H.-Q. Luo, J. Chen, L. Huang, Y.-L. Wang and Q.-Y. Liu, Significant Enhancement of Xe Adsorption and Xe/Kr Separation of Metal–Organic Framework Induced by Pore Channel Shaping and Pore Polarity Engineering, *ACS Materials Lett.*, 2024, **6**, 2809-2815.

[43] X. Wang, F. Ma, S. Xiong, Z. Bai, Y. Zhang, G. Li, J. Chen, M. Yuan, Y. Wang, X. Dai, Z. Chai and S. Wang, Efficient Xe/Kr Separation Based on a Lanthanide–Organic Framework with One-

Dimensional Local Positively Charged Rhomboid Channels, *ACS Appl. Mater. Interfaces*, 2022, **14**, 22233-22241.

[44] P. Zhang, Y. Zhong, Q. Yao, X. Liu, Y. Zhang, J. Wang, Q. Deng, Z. Zeng and S. Deng, Robust Ultramicroporous Metal–Organic Framework with Rich Hydroxyl-Decorated Channel Walls for Highly Selective Noble Gas Separation, *J. Chem. Eng. Data*, 2020, **65**, 4018-4023.

[45] L. Huang, C. Xiong, Y.-L. Wang, X.-P. Fu, L. Chen and Q.-Y. Liu, Metal-organic frameworks with optimal pore cages for high Xe adsorption and efficient Xe/Kr separation, *Sep. Purif. Technol.*, 2025, **352**, 128138.

[46] L. Li, L. Chen, L. Guo, F. Zheng, Z. Zhang, Q. Yang, Y. Yang, B. Su, Q. Ren, J. Li and Z. Bao, Supramolecular Assembly of One-Dimensional Coordination Polymers for Efficient Separation of Xenon and Krypton, *ACS Appl. Mater. Interfaces*, 2023, **15**, 41438-41446.

[47] Y.-S. Bae, B. G. Hauser, Y. J. Colón, J. T. Hupp, O. K. Farha and R. Q. Snurr, High xenon/krypton selectivity in a metal-organic framework with small pores and strong adsorption sites, *Micropor. Mesopor. Mat.*, 2013, **169**, 176-179.

[48] M. T. Kapelewski, J. Oktawiec, T. Runčevski, M. I. Gonzalez and J. R. Long, Separation of Xenon and Krypton in the Metal–Organic Frameworks M_2(m-dobdc) (M=Co, Ni), *Isr. J. Chem.*, 2018, **58**, 1138-1143.

[49] P. K. Thallapally, J. W. Grate and R. K. Motkuri, Facile xenon capture and release at room temperature using a metal–organic framework: a comparison with activated charcoal, *Chem. Commun.*, 2012, **48**, 347-349.

[50] X. Song, Q. Huang, J. Liu, H. Xie, K. B. Idrees, S. Hou, L. Yu, X. Wang, F. Liu, Z. Qiao, H. Wang, Y. Chen, Z. Li and O. K. Farha, Reticular Chemistry in Pore Engineering of a Y-Based Metal–Organic Framework for Xenon/Krypton Separation, *ACS Appl. Mater. Interfaces*, 2023, **15**, 18229-18235.

[51] K. B. Idrees, Z. Chen, X. Zhang, M. R. Mian, R. J. Drout, T. Islamoglu and O. K. Farha, Tailoring Pore Aperture and Structural Defects in Zirconium-Based Metal–Organic Frameworks for Krypton/Xenon Separation, *Chem. Mater.*, 2020, **32**, 3776-3782.

[52] D. Banerjee, C. M. Simon, A. M. Plonka, R. K. Motkuri, J. Liu, X. Chen, B. Smit, J. B. Parise, M. Haranczyk and P. K. Thallapally, Metal–organic framework with optimally selective xenon adsorption and separation, *Nat. Commun.*, 2016, **7**, ncomms11831.

[53] X. Chen, A. M. Plonka, D. Banerjee, R. Krishna, H. T. Schaef, S. Ghose, P. K. Thallapally and J. B. Parise, Direct observation of Xe and Kr Adsorption in a Xe-selective microporous metal–organic framework, *J. Am. Chem. Soc.*, 2015, **137**, 7007-7010.

[54] S. K. Elsaidi, M. H. Mohamed, A. S. Helal, M. Galanek, T. Pham, S. Suepaul, B. Space, D. Hopkinson, P. K. Thallapally and J. Li, Radiation-resistant metal-organic framework enables efficient separation of krypton fission gas from spent nuclear fuel, *Nat. Commun.*, 2020, **11**, 3103.

[55] S. K. Elsaidi, M. H. Mohamed, C. M. Simon, E. Braun, T. Pham, K. A. Forrest, W. Xu, D. Banerjee, B. Space, M. J. Zaworotko and P. K. Thallapally, Effect of ring rotation upon gas adsorption in SIFSIX-3-M (M = Fe, Ni) pillared square grid networks, *Chem. Sci.*, 2017, **8**, 2373-2380.

[56] S.-J. Lee, T.-U. Yoon, A.-R. Kim, S.-Y. Kim, K.-H. Cho, Y. K. Hwang, J.-W. Yeon and Y.-S. Bae, Adsorptive separation of xenon/krypton mixtures using a zirconium-based metal-organic framework with high hydrothermal and radioactive stabilities, *J. Hazard. Mater.*, 2016, **320**,

513-520.

[57] S. Xiong, Q. Liu, Q. Wang, W. Li, Y. Tang, X. Wang, S. Hu and B. Chen, A flexible zinc tetrazolate framework exhibiting breathing behaviour on xenon adsorption and selective adsorption of xenon over other noble gases, *J. Mater. Chem. A*, 2015, **3**, 10747-10752.

[58] Y. Tao, Y. Fan, Z. Xu, X. Feng, R. Krishna and F. Luo, Boosting Selective Adsorption of Xe over Kr by Double-Accessible Open-Metal Site in Metal–Organic Framework: Experimental and Theoretical Research, *Inorg. Chem.*, 2020, **59**, 11793-11800.

[59] L. Yu, S. Xiong, Y. Lin, L. Li, J. Peng, W. Liu, X. Huang, H. Wang and J. Li, Tuning the Channel Size and Structure Flexibility of Metal–Organic Frameworks for the Selective Adsorption of Noble Gases, *Inorg. Chem.*, 2019, **58**, 15025-15028.

[60] Q. Wang, T. Ke, L. Yang, Z. Zhang, X. Cui, Z. Bao, Q. Ren, Q. Yang and H. Xing, Separation of Xe from Kr with Record Selectivity and Productivity in Anion-Pillared Ultramicroporous Materials by Inverse Size-Sieving, *Angew. Chem. Int. Ed.*, 2020, **59**, 3423-3428.

[61] M. Kang, J. H. Choe, H. Kim, H. Yun, D. W. Kim and C. S. Hong, Ultramicroporous hydrogen-bond decorated robust metal–organic framework for high xenon capture performances, *J. Mater. Chem. A*, 2022, **10**, 24824-24830.

[62] Z. Niu, Z. Fan, T. Pham, G. Verma, K. A. Forrest, B. Space, P. K. Thallapally, A. M. Al-Enizi and S. Ma, Self-Adjusting Metal–Organic Framework for Efficient Capture of Trace Xenon and Krypton, *Angew. Chem. Int. Ed.*, 2022, **61**, e202117807.

[63] J.-Z. Wang, X.-P. Fu, Q.-Y. Liu, L. Chen, L.-P. Xu and Y.-L. Wang, Dinuclear Nickel–Oxygen Cluster-Based Metal–Organic Frameworks with Octahedral Cages for Efficient Xe/Kr Separation, *Inorg. Chem.*, 2022, **61**, 5737-5743.

[64] Y.-L. Zhao, X.-Y. Li, X. Bai, M.-Z. Li and X. Zhang, Highly efficient Xe/Kr separation within a metal-organic framework featuring continuous molecule traps, *Chem. Eng. J.*, 2026, **527**, 171349.

[65] H. Wang, M. Warren, J. Jagiello, S. Jensen, S. K. Ghose, K. Tan, L. Yu, T. J. Emge, T. Thonhauser and J. Li, Crystallizing Atomic Xenon in a Flexible MOF to Probe and Understand Its Temperature-Dependent Breathing Behavior and Unusual Gas Adsorption Phenomenon, *J. Am. Chem. Soc.*, 2020, **142**, 20088-20097.